J|A|C|S
ARTICLES

Electronic Structure and Reactivity of Low-Spin Fe(III)−Hydroperoxo Complexes: Comparison to Activated Bleomycin

Nicolai Lehnert,[†,§] Frank Neese,[†,⊥] Raymond Y. N. Ho,[‡] Lawrence Que, Jr.,[‡] and Edward I. Solomon*,[†]

Contribution from the Department of Chemistry, Stanford University, Stanford, California 94305-5080, and Department of Chemistry and Center for Metals in Biocatalysis, University of Minnesota, Minneapolis, Minnesota 55455

Received November 29, 2001

Abstract: The spectroscopic properties, electronic structure, and reactivity of the low-spin Fe(III)−hydroperoxo complex $[Fe(N4Py)(OOH)]^{2+}$ (**1**, N4Py = *N*,*N*-bis(2-pyridylmethyl)-*N*-bis(2-pyridyl)methylamine) are investigated in comparison to those of activated bleomycin (ABLM). Complex **1** is characterized by Raman features at 632 (Fe−O stretch) and 790 cm^{-1} (O−O stretch), corresponding to a strong Fe−O bond (force constant 3.62 mdyn/Å) and a weak O−O bond (3.05 mdyn/Å). The UV−vis spectrum of **1** shows a broad absorption band around 550 nm that is assigned to a charge-transfer transition from the hydroperoxo π_v^* to a t_{2g} d orbital of Fe(III) using resonance Raman and MCD spectroscopies and density functional (DFT) calculations. Compared to low-spin $[Fe(TPA)(OH_x)(OO^tBu)]^{x+}$ (TPA = tris(2-pyridylmethyl)-amine, $x = 1$ or 2), an overall similar Fe−OOR bonding results for low-spin Fe(III)−alkylperoxo and −hydroperoxo species. Correspondingly, both systems show similar reactivities and undergo homolytic cleavage of the O−O bond. From the DFT calculations, this reaction is more endothermic for **1** due to the reduced stabilization of the •OH radical compared to $\bullet O^tBu$ and the absence of the hydroxo ligand that helps to stabilize the resulting Fe(IV)═O species. In contrast, ABLM has a somewhat different electronic structure where no π donor bond between the hydroperoxo ligand and iron(III) is present [Neese, F.; Zaleski, J. M.; Loeb-Zaleski, K.; Solomon, E. I. *J. Am. Chem. Soc.* **2000**, *122*, 11703]. Possible reaction pathways for ABLM are discussed in relation to known experimental results.

Introduction

Bleomycin (BLM) is a glycopeptide antibiotic that is clinically used as an anticancer drug. Its ability to cleave double-stranded DNA is dependent on the availability of reduced metal ions.[1−3] The highest activity is found for iron(II), which is therefore the focus of most research effort. BLM can provide six ligands for binding to iron, but since there is no crystal structure, the existing knowledge of the FeBLM structure is based on spectroscopy and studies on BLM complexes of other metal ions.[2] Fe(II)BLM reacts with dioxygen in the presence of reducing equivalents to form activated bleomycin (ABLM), which is a low-spin end-on Fe(III)−hydroperoxo complex.[4−10] ABLM is competent to cleave DNA by H-atom abstraction from the C_4' position of the DNA ribose sugar. In addition, ABLM is capable of the epoxidation of olefins[11,12] and the hydroxylation of activated aromatic rings.[13]

A number of low-spin Fe(III)−OOH model complexes have been prepared, and their reactivity has been investigated.[14] The PMA ligand of Mascharak et al. closely models BLM, and the corresponding $[Fe(PMA)(OOH)]^+$ intermediate has spectroscopic properties similar to those of ABLM.[15] The low-spin model complex $[Fe(N4Py)(OOH)]^{2+}$ (**1**, N4Py = *N*,*N*-bis(2-

---

* Address correspondence to this author. E-mail: Edward.Solomon@stanford.edu.

[†] Stanford University.

[‡] University of Minnesota.

[§] Current address: Institut für Anorganische Chemie, Christian-Albrechts-Universität Kiel, Olshausenstrasse 40, D-24098 Kiel, Germany.

[⊥] Current address: Max-Planck-Institut für Strahlenchemie, Stiftstrasse 34−36, D-45470 Mülheim an der Ruhr, Germany.

(1) Stubbe, J.; Kozarich, J. W. *Chem. Rev.* **1987**, *87*, 1107−1136.
(2) Stubbe, J.; Kozarich, J. W.; Wu, W.; Vanderwall, D. E. *Acc. Chem. Res.* **1996**, *29*, 322−330.
(3) Burger, R. M. *Chem. Rev.* **1998**, *98*, 1153−1169.
(4) Burger, R. M.; Peisach, J.; Horwitz, S. B. *J. Biol. Chem.* **1981**, *256*, 11636−11644.
(5) Burger, R. M.; Kent, T. A.; Horwitz, S. B.; Münck, E.; Peisach, J. *J. Biol. Chem.* **1983**, *258*, 1559−1564.
(6) Sam, J. W.; Tang, X.-J.; Peisach, J. *J. Am. Chem. Soc.* **1994**, *116*, 5250−5256.
(7) Takahashi, S.; Sam, J. W.; Peisach, J.; Rousseau, D. L. *J. Am. Chem. Soc.* **1994**, *116*, 4408−4413.
(8) Veselov, A.; Sun, H.; Sienkiewicz, A.; Taylor, H.; Burger, R. M.; Scholes, C. P. *J. Am. Chem. Soc.* **1995**, *117*, 7508−7512.
(9) Westre, T. E.; Loeb, K. E.; Zaleski, J. M.; Hedman, B.; Hodgson, K. O.; Solomon, E. I. *J. Am. Chem. Soc.* **1995**, *117*, 1309−1313.
(10) Neese, F.; Zaleski, J. M.; Loeb-Zaleski, K.; Solomon, E. I. *J. Am. Chem. Soc.* **2000**, *122*, 11703−11724.
(11) Heimbrook, D. C.; Carr, S. A.; Mentzer, M. A.; Long, E. C.; Hecht, S. M. *Inorg. Chem.* **1987**, *26*, 3835−3836.
(12) Boger, D. L.; Ramsey, T. M.; Cai, H.; Hoehn, S. T.; Stubbe, J. *J. Am. Chem. Soc.* **1998**, *120*, 9139−9148.
(13) Murugesan, N.; Hecht, S. M. *J. Am. Chem. Soc.* **1985**, *107*, 493−500.
(14) Solomon, E. I.; Brunold, T. C.; Davis, M. I.; Kemsley, J. N.; Lee, S.-K.; Lehnert, N.; Neese, F.; Skulan, A. J.; Yang, Y.-S.; Zhou, J. *Chem. Rev.* **2000**, *100*, 235−349.
(15) Nguyen, C.; Guajardo, R. J.; Mascharak, P. K. *Inorg. Chem.* **1996**, *35*, 6273−6281.

10.1021/ja012621d CCC: $22.00 © 2002 American Chemical Society

pyridylmethyl)-*N*-bis(2-pyridyl)methylamine) has the pentadentate N4Py ligand with four pyridine donors and one *tert*-amine donor which is trans to the hydroperoxide ligand.[16,17] This complex can be deprotonated to yield the corresponding high-spin side-on Fe(III)−peroxo complex,[18] which has also been demonstrated for similar systems.[19,20] This compound converts alkanes with weak C−H bonds (cyclohexane, adamantane, etc.) to alcohols and ketones. Olefins react to afford mainly the corresponding allylic oxidation products, with epoxidation occurring only to a limited extent.[21] In addition, **1** is able to cleave DNA.[22] This reaction has also been observed for a number of other Fe(III)−OOH complexes.[15,23] A different type of reactivity is observed for low-spin [Fe(TPA)(solv)(OOH)]$^{x+}$ (**2**, TPA = tris(2-pyridylmethyl)amine), "solv" is probably water or hydroxide), which shows stereospecific epoxidations and cis-dihydroxylations of olefins and hydroxylations of alkanes.[24−27]

Three different mechanisms have been invoked for the H-atom abstraction reaction of ABLM: (a) heterolytic cleavage of the O−O bond, generating a catalytically active formally Fe(V)═O species; (b) homolytic cleavage, leading to a reactive Fe(IV)═O intermediate; or (c) direct H-atom abstraction by the hydroperoxo complex. The formally Fe(V)═O species formed by heterolytic cleavage of the O−O bond has been observed in heme systems,[28−33] where it is stabilized by oxidation of the porphyrin ligand (P), leading to a ($P^{+\bullet}$)Fe(IV)═O species ("compound I").[34−39] In the case of a non-heme environment, the ligands are much harder to oxidize, which may not provide sufficient stabilization for the high-valent Fe(V)═O species. Therefore, O−O heterolysis has been ruled out for ABLM.[10] Homolotic cleavage of the O−O bond, which leads to the generation of a free •OH radical along with an Fe(IV)═O intermediate, is unlikely for ABLM based on the high kinetic isotope effect (k_H/k_D) of the reaction of ABLM with DNA.[40] On the other hand, O−O homolysis has been shown to occur for low-spin [Fe(TPA)(OH$_x$)(OO^{t}Bu)]$^{x+}$ (^{t}Bu = *tert*-butyl, x = 1 or 2)[41−46] and related systems,[47] low-spin [Fe(PMA)(OO^{t}Bu)]$^+$,[15] and **1**.[21] For ABLM, direct H-atom abstraction from the C−H bond of the DNA sugar has been proposed.[10] This reaction is closely related to the O−O homolysis, having an identical overall reaction energy:

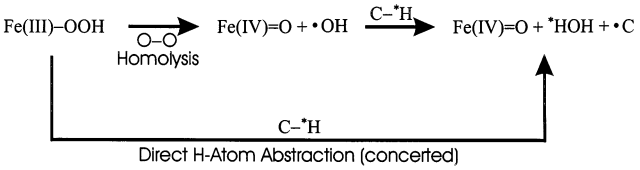

However, the reaction pathway is different, which gives rise to a different potential energy surface and, hence, different kinetics. Therefore, the BLM ligand, which has been proposed to be intermediate between heme and non-heme chemistry,[48] seems to direct the reactivity of ABLM away from O−O homolysis toward direct H-atom abstraction.

This study focuses on the spectroscopic properties, electronic structure, and reactivity of model system **1** in comparison to those of ABLM. Complex **1** shows an intense absorption band at 548 nm (in methanol) and Raman features at 632 and 790 cm^{-1} that have been assigned as the Fe−O and O−O stretches, respectively.[49] Complex **2** has spectroscopic properties that are closely related to those of **1**.[24,49,50] In contrast, no corresponding absorption band is found in the visible region for ABLM, and no Raman features related to the Fe(III)−hydroperoxo group have been obtained.[7,10] These differences in the spectroscopic properties of ABLM and **1** reflect different electronic structures, which can contribute to the different reactivities of these systems (vide supra). This is investigated on the basis of the electronic structure description of **1** which is developed here and that of ABLM.[10] In this respect, we focus on the homolytic cleavage

---

(16) Lubben, M.; Meetsma, A.; Wilkinson, E. C.; Feringa, B.; Que, L., Jr. *Angew. Chem., Int. Ed. Engl.* **1995**, *34*, 1512−1514.
(17) Roelfes, G.; Lubben, M.; Chen, K.; Ho, R. Y. N.; Meetsma, A.; Genseberger, S.; Hermant, R. M.; Hage, R.; Mandal, S. K.; Young, J., V. G.; Zang, Y.; Kooijman, H.; Spek, A. L.; Que, L., Jr.; Feringa, B. L. *Inorg. Chem.* **1999**, *38*, 1929−1936.
(18) Ho, R. Y. N.; Roelfes, G.; Hermant, R.; Hage, R.; Feringa, B. L.; Que, L., Jr. *Chem. Commun.* **1999**, 2161−2162.
(19) Simaan, A. J.; Banse, F.; Mialane, P.; Boussac, A.; Un, S.; Kargar-Grisel, T.; Bouchoux, G.; Girerd, J.-J. *Eur. J. Inorg. Chem.* **1999**, 993−996.
(20) Jensen, K. B.; McKenzie, C. J.; Nielsen, L. P.; Pedersen, J. Z.; Svendsen, H. M. *Chem. Commun.* **1999**, 1313−1314.
(21) Roelfes, G.; Lubben, M.; Hage, R.; Que, L., Jr.; Feringa, B. L. *Chem. Eur. J.* **2000**, *6*, 2152−2159.
(22) Roelfes, G.; Branum, M. E.; Wang, L.; Que, L., Jr.; Feringa, B. L. *J. Am. Chem. Soc.* **2000**, *122*, 11517−11518.
(23) Mialane, P.; Nivorojkine, A.; Pratviel, G.; Azèma, L.; Slany, M.; Godde, F.; Simaan, A.; Banse, F.; Kargar-Grisel, T.; Bouchoux, G.; Sainton, J.; Horner, O.; Guilhem, J.; Tchertanova, L.; Meunier, B.; Girerd, J.-J. *Inorg. Chem.* **1999**, *38*, 1085−1092.
(24) Kim, C.; Chen, K.; Kim, J.; Que, L., Jr. *J. Am. Chem. Soc.* **1997**, *119*, 9, 5964−5965.
(25) Chen, K.; Que, L., Jr. *Chem. Commun.* **1999**, 1375−1376.
(26) Que, L., Jr. Iron-Peroxo and Oxo Complexes modeling Non-heme Iron Enzyme Intermediates. Presented at the 221st ACS National Meeting, San Diego, CA, 2001; Abstract INOR#15.
(27) Chen, K.; Que, L., Jr. *J. Am. Chem. Soc.* **2001**, *123*, 6327−6337.
(28) Groves, J. T. *J. Chem. Educ.* **1985**, *62*, 928−931.
(29) Ortiz-de Montellano, P. R. *Cytochrome P450: Structure, Mechanism and Biochemistry*; Plenum: New York, 1985.
(30) Dawson, J. H. *Science* **1988**, *240*, 433−439.
(31) Traylor, T. G.; Traylor, P. S. *Active Oxygen in Chemistry and Biology*; Blackie Academic and Professional: New York, 1995; p 84.
(32) Sono, M.; Roach, M. P.; Coulter, E. D.; Dawson, J. H. *Chem. Rev.* **1996**, *96*, 2841−2887.
(33) Schlichting, I.; Berendzen, J.; Chu, K.; Stock, A. M.; Maves, S. A.; Benson, D. E.; Sweet, R. M.; Ringe, D.; Petsko, G. A.; Sligar, S. G. *Science* **2000**, *287*, 1615.
(34) Moss, T. H.; Ehrenberg, A.; Bearden, A. J. *Biochemistry* **1969**, *8*, 4159−4162.
(35) Schulz, C. E.; Devaney, P. W.; Winkler, H.; Debrunner, P. G.; Doan, N.; Chiang, R.; Rutter, R.; Hager, L. P. *FEBS Lett.* **1979**, *103*, 102−105.
(36) Penner-Hahn, J. E.; McMurry, T. J.; Renner, M.; Latos-Grazynsky, L.; Smith Eble, K.; Davis, I. M.; Balch, A. L.; Groves, J. T.; Dawson, J. H.; Hodgson, K. O. *J. Biol. Chem.* **1983**, *258*, 12761−12764.
(37) Penner-Hahn, J. E.; Smith Eble, K.; McMurry, T. J.; Renner, M.; Balch, A. L.; Groves, J. T.; Dawson, J. H.; Hodgson, K. O. *J. Am. Chem. Soc.* **1986**, *108*, 7819−7825.
(38) Proniewicz, L. M.; Paeng, I. R.; Nakamoto, K. *J. Am. Chem. Soc.* **1991**, *113*, 3294−3303.
(39) Nakamoto, K. *J. Mol. Struct.* **1997**, *408*, 11−16.
(40) Worth, L., Jr.; Frank, B. L.; Christner, D. F.; Absalon, M. J.; Stubbe, J.; Kozarich, J. W. *Biochem.* **1993**, *32*, 2601−2609.
(41) Arends, I. W. C. E.; Ingold, K. U.; Wayner, D. D. M. *J. Am. Chem. Soc.* **1995**, *117*, 4710−4711.
(42) Kim, J.; Harrison, R. G.; Kim, C.; Que, L., Jr. *J. Am. Chem. Soc.* **1996**, *118*, 4373−4379.
(43) MacFaul, P. A.; Arends, I. W. C. E.; Ingold, K. U.; Wayner, D. D. M. *J. Chem. Soc., Perkin Trans. 2* **1997**, 135−145.
(44) MacFaul, P. A.; Ingold, K. U.; Wayner, D. D. M.; Que, L., Jr. *J. Am. Chem. Soc.* **1997**, *119*, 10594−10598.
(45) Lehnert, N.; Ho, R. Y. N.; Que, L., Jr.; Solomon, E. I. *J. Am. Chem. Soc.* **2001**, *123*, 8271−8290.
(46) Lehnert, N.; Ho, R. Y. N.; Que, L., Jr.; Solomon, E. I. *J. Am. Chem. Soc.* **2001**, *123*, 12802−12816.
(47) Miyake, H.; Chen, K.; Lange, S. J.; Que, L., Jr. *Inorg. Chem.* **2001**, *40*, 3534−3538.
(48) Loeb, K. E.; Zaleski, J. M.; Westre, T. E.; Guajardo, R. J.; Mascharak, P. K.; Hedman, B.; Hodgson, K. O.; Solomon, E. I. *J. Am. Chem. Soc.* **1995**, *117*, 4545−4561.
(49) Ho, R. Y. N.; Roelfes, G.; Feringa, B. L.; Que, L., Jr. *J. Am. Chem. Soc.* **1999**, *121*, 264−265.
(50) It has been speculated that **2** is only five-coordinate, with the terminal oxygen of the hydroperoxide ligand being bound to the open sixth coordination side.[21] However, the fact that this complex is low-spin and that corresponding side-on Fe(III)−peroxo complexes are high-spin [18−20,51] argues against this.

of the O−O bond. By comparing the three complexes **1**, **2**, and ABLM, further insight is obtained into how different ligand sets influence the energetics of O−O homolysis.

Experimental and Computational Procedures

The Fe(III)−hydroperoxo complex **1** was prepared following the general procedure described in ref 16.

UV−Vis Spectroscopy. Absorption spectra have been recorded in methanol solution at −20 °C on a Hewlett-Packard 8452 diode array spectrophotometer.

Raman Spectroscopy. Resonance Raman spectra were measured at an excitation wavelength of 615 nm in frozen methanol solutions at 77 K. An Acton AM-506 spectrometer with a Princeton Instruments CCD detector (LN-1100PB) was used together with a Spectra Physics 2030-15 argon ion laser to pump a 375B CW dye laser (rhodamine 6G). The mixed-isotope-labeled ($^{18}O^{16}O$) data were measured at 568 nm excitation using the argon laser. Spectra were recorded in a backscattering geometry.

For the resonance Raman profiles, a series of excitation wavelengths of a krypton ion (Coherent 190C-K) and an argon ion (Coherent Sabre 25/7) laser have been used at incident powers of about 25 mW and in a ∼135° backscattering geometry. A Spex 1877 CP triple monochromator (equipped with 1200, 1800, and 2400 grooves/mm gratings) has been used together with a back-illuminated CCD camera (Princton Instruments LN/CCD-1100PB) as a detector. Samples were measured at 77 K. Raman intensities were internally calibrated to the intense 1034 cm^{-1} vibration of the solvent methanol. Sample concentrations were in the range of ∼10 mM.

MCD Spectroscopy. MCD spectra have been obtained on frozen glasses of methanol/ethylene glycol solutions at liquid He temperatures (1.8−25 K). For the UV−vis energy region, a CD spectropolarimeter (Jasco 810) with S1 and S20 photomultiplier tubes has been used where the sample compartment was modified to accommodate an Oxford Instruments SM4-7T magnetocryostat. The NIR MCD spectra were recorded on a Jasco 200 spectropolarimeter with an Oxford SM4000-7T magnetocryostat using an InSb detector. The samples were frozen in metallic sample compartments between two Infrasil quartz disks separated by 3 mm neoprene spacers. Typical sample concentrations were in the range of 1.0 mM and ∼5 mM for the NIR experiment.

Data Analysis. Normal coordinate calculations were performed using the QCPE computer program 576 by M. R. Peterson and D. F. McIntosh, which involves solution of the secular equation $\mathbf{GFL} = \lambda\mathbf{L}$ by the diagonalization procedure of Miyazawa.[52] The calculations are based on a general valence force field; force constants are refined with the nonlinear optimization routine of the simplex algorithm according to Nelder and Mead.[53] The simplex optimization was used to refine only *selected* force constants according to the quantum-chemical assisted normal coordinate analysis.[54] Here, a force field from DFT calculations is used as a starting point to generate initial force constants, and a subset of these is fit to reproduce the known experimental frequencies.

Density Functional Calculations. Spin-unrestricted DFT calculations using Becke's three-parameter hybrid functional with the correlation functional of Lee, Yang, and Parr (B3LYP[55]) were performed using the program package Gaussian 94/98.[56] The structure of the Fe(III)−hydroperoxo model system low-spin $[Fe(NH_3)_5(OOH)]^{2+}$ ($\tilde{\mathbf{1}}$) was fully optimized using the LanL2DZ basis set and, in addition, the SDD, a mixed 6-311G (Fe)/6-31G (all other atoms), the TZV,[57] and the DZVP-DFT[58] basis sets. To explore ligand effects, the structures of the model low-spin $[Fe(Ime)_4(NH_3)(OOH)]^{2+}$ (Ime = imine, $CH_2{=}NH$) and of the complete molecule low-spin $[Fe(N4Py)(OOH)]^{2+}$ (**1**) have been fully optimized by applying the LanL2DZ basis set. In addition, the model low-spin $[Fe(NH_3)_4(OH)(OOH)]^+$ ($\tilde{\mathbf{2}}$) and two $[(NH_3)_5Fe^{IV}{=}O]^{2+}$ ($S = 1, 2$) intermediates were fully optimized using LanL2DZ. The model for ABLM was taken from ref 10 (cf. Supporting Information Figure 3), and its structure as well as that of the corresponding $Fe^{IV}{=}O$ intermediate ($S = 1$) were fully optimized using the LanL2DZ basis set. Vibrational frequencies as well as thermodynamic parameters[59] have been calculated for all species. The structures of the $[(NH_3)_4(OH)Fe^{IV}{=}O]^+$ ($S = 1,2$) intermediates were taken from ref 46. The LanL2DZ basis set applies Dunning/Huzinaga full double-ζ (D95)[60] basis functions on first row atoms and Los Alamos effective core potentials plus DZ functions on all other atoms.[61] For the calculations of the reaction energies, the TZV basis set has also been applied on the LanL2DZ structures. Solvation effects were included in the calculations using the polarized continuum model (PCM).[62] Acetonitrile was used as the solvent for the model systems in order to obtain thermodynamic data that can directly be compared to related studies on Fe(III)−alkylperoxo complexes[45,46] (note that the dielectric constants of methanol ($\epsilon = 33$) and acetonitrile ($\epsilon = 37$) are comparable). For ABLM, water ($\epsilon = 78$) has been used as solvent. In all these calculations, convergence was reached when the relative change in the density matrix between subsequent iterations was less than 1×10^{-8}. Force constants in internal coordinates were extracted from the Gaussian output using the program Redong[63] (QCPE 628). For the calculation of the O−O bond homolysis in ABLM, the following selected parameters have been reoptimized at every O−O distance using B3LYP/LanL2DZ (r = bond distance, $\angle$ = angle): r(Fe−O), r(O−H), the r(Fe−N)'s of the two ammonias, and the corresponding metal−ligand angles, ∠Fe−O−O and ∠O−O−H.

The MO diagram of $\tilde{\mathbf{1}}$ was obtained from spin-unrestricted calculations that have been performed with the Amsterdam Density Functional (ADF) program version 2.0.1[64] using the local density approximation (LDA) together with gradient corrections for exchange (Becke88[65]) and correlation (Perdew86[66]). An uncontracted valence triple-ζ Slater-type basis set was used (ADF basis set IV) for all atoms, with an additional set of f functions (exponent $\alpha = 1.5$) on iron. Core orbitals through 1s (C, N, O) and 3p (Fe) were frozen in the calculations. Orbitals were plotted with the program Cerius2.

Time-dependent DFT (TD-DFT) calculations within the Tamm-Dancoff approximation (TDA) were carried out with the program ORCA.[67] The TDA has recently been shown to provide a good approximation to the full TD-DFT treatment of excitation energies.[68] The calculations were carried out on the optimized geometries of $\tilde{\mathbf{1}}$ and, for consistency, employed the BP functional and the accurate

---

(51) Neese, F.; Solomon, E. I. *J. Am. Chem. Soc.* **1998**, *120*, 12829−12848.

(52) Miyazawa, T. *J. Chem. Phys.* **1958**, *29*, 246.

(53) Nelder, J. A.; Mead, R. *Computer J.* **1965**, *7*, 308.

(54) Lehnert, N.; Tuczek, F. *Inorg. Chem.* **1999**, *38*, 1659−1670.

(55) (a) Becke, A. D. *Phys. Rev. A* **1988**, *38*, 3098. (b) Becke, A. D. *J. Chem. Phys.* **1993**, *98*, 1372. (c) Becke, A. D. *J. Chem. Phys.* **1993**, *98*, 5648.

(56) Frisch, M. J.; Trucks, G. W.; Schlegel, H. B.; Gill, P. M. W.; Johnson, B. G.; Robb, M. A.; Cheeseman, J. R.; Keith, T. A.; Petersson, G. A.; Montgomery, J. A.; Raghavachari, K.; Al-Laham, M. A.; Zakrzewski, V. G.; Ortiz, J. V.; Foresman, J. B.; Cioslowski, J.; Stefanov, B. B.; Nanayakkara, A.; Challacombe, M.; Peng, C. Y.; Ayala, P. Y.; Chen, W.; Wong, M. W.; Andres, J. L.; Replogle, E. S.; Gomperts, R.; Martin, R. L.; Fox, D. J.; Binkley, J. S.; Defrees, D. J.; Baker, J.; Stewart, J. P.; Head-Gordon, M.; Gonzalez, C.; Pople, J. A. *Gaussian 94/98*; Gaussian, Inc.: Pittsburgh, 1995.

(57) For these, see references in the following: Frisch, Æ.; Frisch, M. J. *Gaussian 98 User's Reference*; Gaussian, Inc.: Pittsburgh, 1999.

(58) Godbout, N.; Salahub, D. R.; Andzelm, J.; Wimmer, E. *Can. J. Chem.* **1992**, *70*, 560.

(59) Ochterski, J. W. *Thermochemistry in Gaussian*, 2000; available free of charge at www.gaussian.com

(60) *Modern Theoretical Chemistry*; Dunning, T. H., Jr.; Hay, P. J.; Schaefer, H. F., III, Eds.; Plenum: New York, 1976.

(61) (a) Hay, P. J.; Wadt, W. R. *J. Chem. Phys.* **1985**, *82*, 270 and 299. (b) Wadt, W. R.; Hay, P. J. *J. Chem. Phys.* **1985**, *82*, 284.

(62) Cramer, C. J.; Truhlar, D. G. *Chem. Rev.* **1999**, *99*, 2161−2200.

(63) Allouche, A.; Pourcin, J. *Spectrochim. Acta* **1993**, *49A*, 571.

(64) (a) Baerends, E. J.; Ellis, D. E.; Ros, P. *J. Chem. Phys.* **1973**, *2*, 42. (b) te Velde, G.; Baerends, E. J. *J. Comput. Phys.* **1992**, *99*, 84.

(65) Becke, A. D. *J. Chem. Phys.* **1986**, *84*, 4524.

(66) Perdew, J. P.; Chevary, J. A.; Vosko, S. H.; Jackson, K. A.; Pederson, M. R.; Singh, D. J.; Fiolhais, C. *Phys. Rev. A* **1992**, *46*, 6671.

(67) Neese, F. ORCA−an ab initio, Density Functional and Semiempirical Program Package, Version 2.1, revision 76, Max Planck Institut für Strahlenchemie, Mülheim, October 2001.

(68) Hirata, S.; Head-Gordon, M. *Chem. Phys. Lett.* **1999**, *314*, 291.

Chart 1

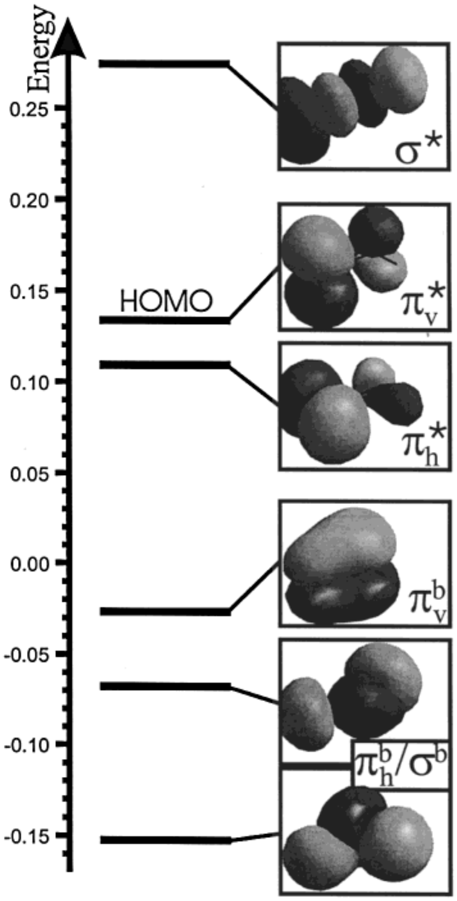

Ahlrichs polarized valence triple-ζ (VTZP) basis set[69] for all atoms. The first 20 excited states states were determined.

Chart 1 shows the molecular orbital (MO) diagram of the free OOH^- ligand with the nomenclature of the different orbitals. At highest energy is the antibonding combination of the oxygen p functions that point along the O−O bond, labeled σ*, which is unoccupied. The highest occupied molecular orbital (HOMO) of hydroperoxide is the antibonding combination of the oxygen p functions that are oriented perpendicular to the O−O−H plane. This orbital is labeled π_v^* (v for vertical). Close in energy is π_h^* (h for horizontal), which is the corresponding antibonding combination of the oxygen p functions that are located within the O−O−H plane. Importantly, this orbital has almost no contribution from the hydrogen. At lower energy are the corresponding bonding MOs of these orbitals, π_v^b, π_h^b, and σ^b. Note that π_h^b and σ^b are strongly mixed in the free hydroperoxo ligand, but this is no longer the case in the iron(III) complex (vide infra). The orbitals π_v^* and π_v^b are potential π donors to the t_{2g} d orbitals of iron, whereas π_h^*, π_h^b, and σ^b can undergo σ interactions with the e_g d orbitals. Note that the MO diagram of hydroperoxide is very similar to that of $^tBuOO^-$.[45]

Results and Analysis

A. Spectroscopy. A.1. Resonance Raman Spectra and Vibrational Analysis. Vibrational Assignment. Figure 1 shows the resonance Raman spectra of low-spin $[Fe(N4Py)(OOH)]^{2+}$ (**1**). In the natural abundance isotopes (NAI) spectrum in the top panel, four bands are observed at 632, 652, 673, and 790 cm^{-1}. On ^{18}O substitution, the 632 and 790 cm^{-1} modes shift to 616 and 746 cm^{-1}, respectively. The two peaks at 652 and 673 cm^{-1} show only small shifts of <5 cm^{-1}, but they distincly lose intensity on ^{18}O isotope labeling. This indicates that these two modes gain their resonance intensity from mixing with the 632 cm^{-1} vibration. The shift of the 632 cm^{-1} mode to lower energy then decreases this mixing and, hence, the intensity of the 652 and 673 cm^{-1} peaks. On deuteration, no shift is observed for the 790 cm^{-1} mode, whereas the 632 cm^{-1} feature shifts 5 cm^{-1} to lower energy. On the basis of these data, the 790 and 632 cm^{-1} peaks have been assigned to the O−O and Fe−O stretches, respectively.[49] The bands at 652 and 673 cm^{-1} do not correspond to vibrations of the Fe(III)−OOH subunit (see NCA result below); hence, they are identified with vibrations of the N4Py ligand. From the ^{18}O isotope effects on their intensity, these mix with the Fe−O stretch. Figure 1 also contains data for mixed-isotope-labeled peroxide, which initially consists of a 1:2:1 mixture of $H^{16}O^{16}OH : H^{16}O^{18}OH : H^{18}O^{18}OH$. On complexation to Fe(III), this gives rise to four different species. These data are analyzed below. The model complex $[Fe(TPA)(solv)(OOH)]^{x+}$ (**2**) has very similar resonance Raman features, with ν(FeO) at 626 cm^{-1} and ν(OO) at 789 cm^{-1}.[49] Importantly, in this case no additional peaks corresponding to the 652 and 673 cm^{-1} features of **1** are observed, which is consistent with these modes being associated with the N4Py ligand.

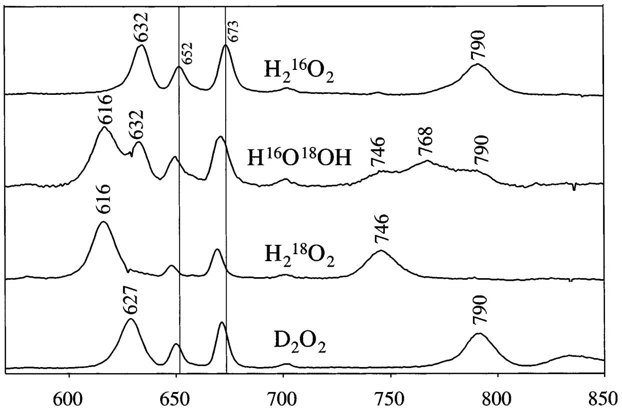

Figure 1. Resonance Raman spectra of **1**. From top to bottom: natural abundance isotopes (NAI) spectrum; spectrum with mixed-oxygen-isotope-labeled H_2O_2; spectrum with ^{18}O-labeled peroxide; spectrum with deuterated peroxide.

To quantitatively analyze the vibrational spectra of **1**, determine force constants of important bonds, and understand the mixed-isotope-labeled spectrum in Figure 1, a normal coordinate analysis (NCA) has been performed on a simplified model of **1**. As the crystal structure of **1** is not known, a model having the five nitrogen donors of the N4Py ligand substituted by NH_3 ($\tilde{\mathbf{1}}$) was geometry optimized using density functional (DFT) calculations (vide infra). The resulting structure is shown in Figure 2. For the NCA, all hydrogen atoms of the ammonias are neglected, leading to model $\hat{\mathbf{1}}$ that consists of the eight heavy atoms of $\tilde{\mathbf{1}}$ and the hydrogen atom of the ^-OOH ligand (Figure 2 and cf. Supporting Information Table 2). Effective masses reflecting the N4Py ligand are used for the nitrogens ($M = 50$ for N_5, $M = 74$ for N_6-N_9). The calculated force field of $\tilde{\mathbf{1}}$ was used as a first approximation for NCA, and then selected force constants were fitted to reproduce the experimental results (QCA-NCA[54]). Since the sample with the mixed-isotope-labeled peroxide contains several different species, it was excluded from the NCA fit. Supporting Information Table 1 gives the force

---

[69] Schäfer, A.; Huber, C.; Ahlrichs, R. J. *Chem. Phys.* **1994**, *100*, 5829.

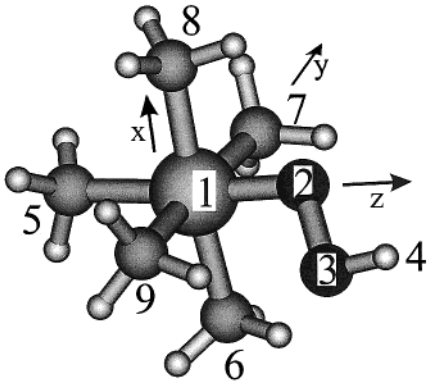

Figure 2. Optimized structure (B3LYP/LanL2DZ) of the simplified model $\hat{\mathbf{1}}$ in which the N4Py ligand has been replaced by five ammonias (see text). The coordinates of $\hat{\mathbf{1}}$ are given in Supporting Information Table 2. Important structural parameters (bond lengths in angstroms, angles in degrees) are: $r(\mathrm{Fe{-}O}) = 1.821$; $r(\mathrm{O{-}O}) = 1.493$; $\angle \mathrm{Fe{-}O{-}O} = 112$; $\angle \mathrm{H{-}O{-}O} = 103$; $\angle \mathrm{Fe{-}O{-}O{-}H} = 179$. The eight heavy atoms of this system and the hydrogen of the $^{-}$OOH ligand comprise the model used for NCA ($\hat{\mathbf{1}}$) with the indicated numbering of the atoms.

Table 1. Comparison of Experimental and QCA−NCA Frequencies and Potential Energy Distributions

exptl frequency	QCA–NCA frequency	potential energy distribution			
		ΔFe–O	ΔO–O	∠Fe–O–O	∠O–O–H
		$\mathrm{Fe{-}{}^{16}O{-}{}^{16}O{-}H}$ (NAI)			
	1282	1	0	1	99
790	791	15	76	1	5
632	633	62	7	23	1
		$\mathrm{Fe{-}{}^{18}O{-}{}^{18}O{-}H}$			
	1275	0	0	0	99
746	746	16	75	1	4
616	607	60	8	22	1
		$\mathrm{Fe{-}{}^{16}O{-}{}^{16}O{-}D}$			
	952	4	0	2	93
790	789	13	75	1	7
627	625	63	6	22	0
		$\mathrm{Fe{-}{}^{16}O{-}{}^{18}O{-}H}$ (simulated)[a]			
	775	18	73	1	5
	631	59	8	24	1
		$\mathrm{Fe{-}{}^{18}O{-}{}^{16}O{-}H}$ (simulated)[a]			
	764	13	78	1	5
	608	63	6	22	1

[a] The spectrum of the mixed-isotope-labeled compound corresponds to a mixture of different species. Therefore, these data have been simulated but not fit in the QCA−NCA procedure (see text).

constants of the Fe−O−O−H subunit of $\hat{\mathbf{1}}$ before (column labeled "calc") and after (QCA-NCA) fitting to the experimental data. The potential energy distributions from the QCA-NCA fit of $\hat{\mathbf{1}}$ for the NAI complex and the ^{18}O and D isotope-substituted species are given in Table 1, along with a comparison of the experimental and predicted vibrational energies. As indicated in Supporting Information Table 1, only three force constants need to be fit to obtain very good agreement of the calculated vibrational frequencies with experiment.

The results from the NCA are consistent with the previous assignment of the 790 cm^{-1} peak to ν(OO) and the 632 cm^{-1} feature to ν(FeO). The observed isotope shifts of these modes are well reproduced by the NCA, as shown in Table 1. In the simulation, ν(OO) is an almost pure vibration, with ~75% ΔO−O character and only 15% admixture from the Fe−O stretch. In contrast, ν(FeO) is more mixed and contains 22% of the Fe−O−O bend. Note that the O−O−H bending vibration is located at higher energy (~1280 cm^{-1}) and does not mix with ν(OO) or ν(FeO), which explains why this mode is not resonance enhanced.

The spectrum of the mixed-isotope-labeled peroxide in Figure 1 shows peaks at 790 and 632 cm^{-1} as well as 746 and 632 cm^{-1} which belong to the NAI and the ^{18}O-labeled complexes, respectively, that are also present in the mixture. The only new feature is a very broad band that appears to be centered around 768 cm^{-1}. Using the force field obtained from the NCA fit, the vibrational energies of the two mixed-isotope-labeled species, $\mathrm{Fe{-}{}^{16}O{-}{}^{18}O{-}H}$ and $\mathrm{Fe{-}{}^{18}O{-}{}^{16}O{-}H}$, can be predicted. As shown in Table 1, the O−O stretches of these two species are located at 775 and 764 cm^{-1}, respectively, which is intermediate between the NAI and the ^{18}O-labeled compound. This explains the occurrence of the broad feature around 768 cm^{-1} in the spectrum, which would be a superposition of these two O−O stretches. The Fe−O stretches of the $\mathrm{Fe{-}{}^{16}O{-}{}^{18}O{-}H}$ (at 631 cm^{-1}) and the $\mathrm{Fe{-}{}^{18}O{-}{}^{16}O{-}H}$ (at 608 cm^{-1}) species practically overlay the Fe−O stretches of the NAI (at 633 cm^{-1} in the NCA) and the ^{18}O-labeled (at 607 cm^{-1} in the NCA) complexes, which explains the lack of an extra feature in this energy region in the mixed-isotope spectrum.

Analysis of Force Constants. The calculated force constants for the Fe−O and O−O bonds show an interesting behavior, where the Fe−O bond ($k = 3.62$ mdyn/Å) is stronger than the O−O bond ($k = 3.05$ mdyn/Å). This is in agreement with the experimental order of bond strengths that has been found for the related low-spin Fe(III)−OO^{t}Bu complex [Fe(TPA)(OH$_x$)(OO^{t}Bu)]$^{x+}$,[45] as shown in Table 2. In agreement with the similar force constants, both compounds have about the same O−O stretching frequencies (790 vs 796 cm^{-1}). However, the vibrational energies of the Fe−O stretch are very different: for **1**, ν(FeO) is located at 632 cm^{-1}, whereas the Fe(III)−OO^{t}Bu complex has an Fe−O stretching frequency of 696 cm^{-1}. Insight into the origin of this difference comes from a simulation where the force field and the coordinates of the Fe(III)−OO^{t}Bu complex from ref 45 are used and the $^{-}$OOH group is projected onto the O−O−C subunit of the $^{-}$OO^{t}Bu ligand and, correspondingly, the **f** matrix is truncated.[70] In this case (model ls-[Fe(N$_4$)(O)(OOH)] in Table 2), the Fe−O stretch is located at 626 cm^{-1}, compared to the 696 cm^{-1} of the initial Fe(III)−OO^{t}Bu complex. Therefore, the increased vibrational energy of ν(FeO) in the *tert*-butylperoxo complex compared to that of the hydroperoxo complex reflects the strong interaction of the Fe−O stretch with vibrations of the OC(CH$_3$)$_3$ group (cf. ref 45) that are not present in the hydroperoxo complex. Importantly, these very different vibrational frequencies for ν(FeO) represent comparable Fe−O force constants and, hence, bond strengths. This indicates that the electronic structures of the low-spin Fe(III)−OOH model complexes **1** and **2** are closely related to that of the low-spin Fe(III)−OO^{t}Bu system.

A.2. UV−Vis Absorption, MCD, and Resonance Raman Profiles. Figure 3, top, shows the absorption spectrum of **1** recorded in methanol solution. A broad absorption band is observed around 18 200 cm^{-1} (550 nm; $\epsilon = 1200$ M^{-1} cm^{-1}). At higher energy, an additional feature is found at about 26 500 cm^{-1}. No further distinct absorption band can be identified from

---

(70) Some force constants of the original Fe(III)−OO^{t}Bu force field need to be adjusted, since, for example, the O−H force constant is very different from that of the O−C bond.

Table 2. Calculated (B3LYP/LanL2DZ) and Experimental Frequencies and Force Constants

	force constant (mdyn/Å)			frequency (cm^{-1})		
calcd/**exptl**	Fe–O	O–O	C–O	Fe–O	O–O	ref
calc: HOOH		4.40			905	45
NCA: HOOH[a]		4.01			880	
calc: HOO^-		3.08			750	45
exp: HOO^-[b]					775	
calc: $^-O-O^-$		1.94			641	45
calc: ls-$[Fe(NH_3)_5(OOH)]^{2+}$	3.25	3.93		575	879/897	*c*
NCA: ls-$[Fe(N4Py)(OOH)]^{2+}$	**3.62**	**3.05**		**632**	**790**	*c*
NCA: ls-$[Fe(TPA)(OH_x)(OO^tBu)]^{x+}$	**3.53**	**2.92**	**2.83**	**696**	**796**	45
Sim: ls-$[Fe(N_4)(O)(OOH)]$[d]	3.53	2.92		626	778	*c*
NCA: hs-$[Fe(TPA)(OH_x)(OO^tBu)]^{x+}$	**2.87**	**3.55**	**2.45**	**637**	**860**[e]	46

[a] Measured in the gas phase.[85] [b] Determined with photoelectron spectroscopy in the gas phase;[86] the error of this value is ±250 cm^{-1}. Calculations (GVB-CI) lead to values of 777−820 cm^{-1} for ν(OO). [c] This work. [d] This simulation is based on the coordinates and the force field of ls-$[Fe(TPA)(OH_x)(OO^tBu)]^{x+}$,[45] where the OOH ligand is projected on the O−O−C subunit of the OO^{t}Bu group (see text). The vibrational energies are obtained after adjusting the O−O−H bending and O−H stretching force constants and some related nondiagonal elements. [e] The O−O stretching frequency in the deuterated compound, where mode mixing with ν_s(CC) is small.

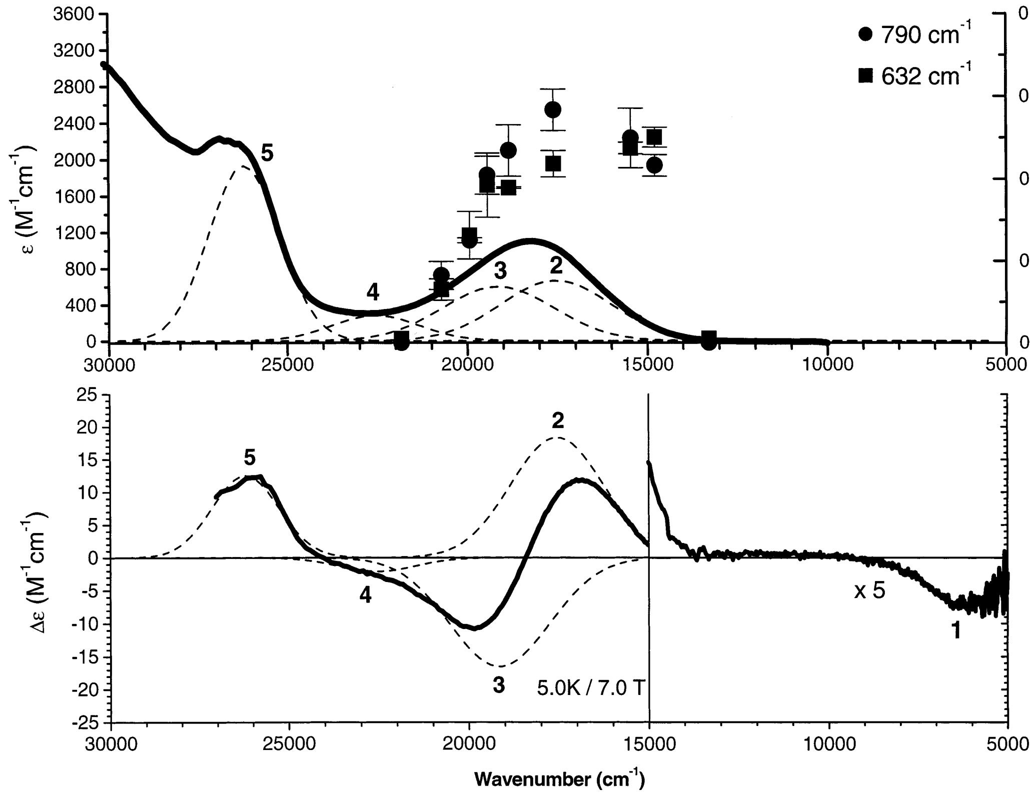

Figure 3. UV−vis (top) and MCD spectra (bottom; recorded at 5 K and 7 T) of **1** together with a correlated Gaussian fit (bands 1−5). The low energy range of the MCD spectrum (bottom, right) is enlarged by a factor of 5. The UV−vis panel on the top also contains the resonance Raman profiles of ν(FeO) (■; 632 cm^{-1}) and ν(OO) (●; 790 cm^{-1}).

Table 3. Result of the Simultaneous Gaussian Fit of the Absorption and MCD Spectra

band	ν_{max} (cm^{-1})	ϵ_{max} (M^{-1} cm^{-1})	$\Delta\epsilon_{max}$ (M^{-1} cm^{-1})	*f*[a]	$\|\Delta\epsilon/\epsilon\|$
1	6 169		−1		
2	17 542	666	18	0.01105	0.027
3	19 149	599	−17	0.01005	0.028
4	22 552	282	−2	0.00366	0.007
5	26 200	1 934	13	0.02086	0.007

[a] Oscillator strength.

the spectrum. The resonance Raman profiles of the Fe−O and the O−O stretch at 632 and 790 cm^{-1}, respectively, are shown in Figure 3, top. Both vibrations are clearly resonance enhanced with respect to the 550 nm absorption band, which therefore can be assigned as a hydroperoxo-to-Fe(III) charge-transfer (CT) transition (cf. section B). Unfortunately, complex **1** is not stable to laser irradiation below 550 nm. Hence, the shapes of the profiles at higher energy are uncertain, and a fit of the resonance Raman profiles with time-dependent Heller theory could not be performed.

The low-temperature MCD spectrum of **1** shown in Figure 3, bottom, allows the identification of additional transitions. The five Gaussians in Figure 3 correspond to a simultaneous fit of the absorption and MCD spectra of **1**. The resulting fit parameters are given in Table 3. A very weak MCD feature is observed around 6200 cm^{-1} (band 1 in Figure 3), just above

Table 4. Comparison of Relative Donor Strengths and Fe−O Force Constants of Fe(III)−Peroxo Complexes

complex	$\pi^* \rightarrow$ d CT (cm^{-1})	donor strength $(C^{M}_{\pi^*})^2$ ratio[a]	ν_{Fe-O} (cm^{-1})	k_{Fe-O} (mdyn/Å)	ν_{O-O} (cm^{-1})	k_{O-O} (mdyn/Å)	ref
ls-Fe(TPA)OO^{t}Bu	16 000 17 364	0.5	696	3.53	796	2.92	45
hs-Fe(6-Me$_3$TPA)OO^{t}Bu	18 123	0.5	637	2.87	860[b]	3.55	46
ls-Fe(N4Py)OOH	17 542 19 149	0.23	632	3.62	790	3.05	c

[a] Corresponds to the charge donation of peroxide to the metal. This value is relative to the donor strength of the $\pi^* \rightarrow$ d CT transition of a Cu−peroxo end-on monomer (set to 1.0).[87] [b] The O−O stretching frequency in the deuterated compound, where mode mixing with ν_s(CC) is small. [c] This work.

Table 5. Calculated (B3LYP/LanL2DZ) Geometries and Properties[a] of Models for Low-Spin [Fe(N4Py)(OOH)]$^{2+}$ (**1**), Low-Spin [Fe(TPA)(OH$_x$)(OOH)]$^{x+}$ (**2**), and ABLM

	geometric parameters									
molecule	r(Fe–O)	r(O–O)	r(Fe–N$_{tr}$)	r(Fe–N$_c$)[b]	∠FeOO	∠OOH	ν(FeO)	k(FeO)	ν(OO)	k(OO)
ls-[Fe(NH$_3$)$_5$(OOH)]$^{2+}$	1.821	1.493	2.072	2.054	112	103	575	3.25	879/897	3.93
ls-[Fe(Ime)$_4$(NH$_3$)(OOH)]$^{2+}$ [c]	1.822	1.489	2.053	1.998	112	103	609	3.15	884	3.91
ls-[Fe(N4Py)(OOH)]$^{2+}$	1.804	1.490	2.033	1.996	117	102	606		879	
ls-[Fe(NH$_3$)$_4$(OH)(OOH)]$^{+}$	1.845	1.507	2.053[d]		112	102	518[e]		887	
ABLM″	1.832	1.498			115	101	540		890	

[a] For charges and spin densities, see Supporting Information Table 10. [b] Average of the Fe−N distances of the four ligands cis to hydroperoxide. [c] Ime = Imine ligand H−N═CH$_2$ as a model for pyridine. [d] Average of all Fe−N distances. [e] Lowered in energy by interaction with ν(Fe−OH) at 588 cm^{-1}.

the detection limit of the IR MCD instrument. This corresponds to the highest energy $t_{2g} \rightarrow t_{2g}$ transition within the $[t_{2g}]^5$ subshell of low-spin iron(III). The energy of this feature can be calculated from the observed g values (2.17, 2.12, 1.98 for **1**; cf. ref 16) using a formalism developed by Taylor.[71] Applying second-order perturbation theory, simple formulas for the relative g-shifts, Δg, are obtained:[10]

$$\Delta g_{\max} = \frac{2\zeta}{V}$$

$$\Delta g_{\mathrm{mid}} = \frac{4\zeta}{2\Delta + V}$$

with ζ being the spin−orbit coupling (SOC) constant and Δ and V being the t_{2g} orbital splittings. Using $\zeta = 380$ cm^{-1} for the 3d orbitals of Fe(III) and $\Delta = 4190$ cm^{-1} and $V = 4530$ cm^{-1} obtained from the g shifts, the highest energy $t_{2g} \rightarrow t_{2g}$ transition is calculated to be at 6455 cm^{-1}, which is in good agreement with experiment. At higher energy, the broad absorption feature around 550 nm is resolved into an intense pseudo-**A** signal in the MCD spectrum (bands 2 and 3). These spectral features are very similar to the MCD spectrum of the related low-spin [Fe(TPA)(OH$_x$)(OO^{t}Bu)]$^{x+}$ complex.[45] Correspondingly, the pseudo-**A** term is attributed to the configuration interaction (CI) mixing of the excited hydroperoxo-to-iron CT state with a ligand field excited state of type $t_{2g} \rightarrow e_g$. Both resulting states Ψ_1 and Ψ_2 are about equal mixtures of these initial states. In order for MCD intensity to arise, Ψ_1 and Ψ_2 have to spin−orbit couple to another $t_{2g} \rightarrow e_g$ ligand field excited state. This latter state is of lower MCD intensity than the pseudo-**A** signal and could correspond to band 4 in Figure 3. The fact that this "three-state model" [45] can be successfully applied to the MCD spectra of **1** and of low-spin [Fe(TPA)(OH$_x$)(OO^{t}Bu)]$^{x+}$ indicates that the electronic structures of the Fe(III)−OOR (R = H, ^{t}Bu) subunits are very similar in these complexes. Finally, band 5 in the Gaussian fit in Figure 3 corresponds to the absorption around 26 500 cm^{-1} mentioned above. In comparison to low-spin [Fe(TPA)(OH$_x$)(OO^{t}Bu)]$^{x+}$,[45] this feature can be assigned as a pyridine-to-Fe(III) CT transition. The alternative assignment of this band to a peroxo-to-Fe(III) CT has been ruled out on the basis of resonance Raman data and calculated excitation energies.[45]

A.3. Donor Strength of the Charge-Transfer State. Using the formalism of Baldwin et al.,[72] the donor strength of a ligand is approximately given by

$$(C^{M}_{\pi^*})^2 = 9.22 \times 10^{-2}\ \text{Å} \times \sum_i \frac{f_i}{\nu_i |\mathbf{r}|^2}$$

with f being the oscillator strength and ν the frequency of the ith charge-transfer band, and **r** is the transition vector that coincides with the Fe−O bond and can be set to the Fe−O bond length. This equation relates the metal d orbital contributions to the ligand donor orbitals and therefore the strength of the metal−ligand bond to the intensity of the resulting CT transition. The donor strength is calibrated relative to the value obtained for an end-on Cu−peroxide monomer whose donor strength has been set to 1.0. For complex **1**, a low value of 0.23 is calculated for combined bands 2 and 3, corresponding to the hydroperoxo-to-Fe(III) CT transition in the visible spectral region. Importantly, as shown in Table 4, this is about half the value for low-spin [Fe(TPA)(OH$_x$)(OO^{t}Bu)]$^{x+}$, which indicates that the corresponding Fe−O bond is distinctly weaker in **1** (see Discussion).

B. Density Functional Calculations. B.1. Geometry and Evaluation Based on Calculated Spectral Features. To calculate the electronic structure of **1**, the simplified model [Fe(NH$_3$)$_5$(OOH)]$^{2+}$ ($\tilde{\mathbf{1}}$) has been fully optimized with different basis sets (cf. Supporting Information Table 10). Using the effective core potential (ECP) basis set LanL2DZ, a reasonable structure with an Fe−O distance of 1.821 Å and an O−O bond

---

(71) Taylor, C. P. S. *Biochim. Biophys. Acta* **1977**, *491*, 137−149.
(72) Baldwin, M. J.; Root, D. E.; Pate, J. E.; Fujisawa, K.; Kitajima, N.; Solomon, E. I. *J. Am. Chem. Soc.* **1992**, *114*, 10421.

length of 1.493 Å is obtained (cf. Figure 2 and Table 5). This is in agreement with the crystal structure of $[Cu(L_1)(OOCm)]$[73] and the calculated structure of low-spin $[Fe(TPA)(OH_x)(OO^tBu)]^{x+}$.[45] The frequencies and force constants obtained show some deviations from experiment. Particularly, the calculated O−O force constant of 3.93 mdyn/Å is much larger than experimentally determined (3.05 mdyn/Å). Applying the SDD (ECP) basis set (cf. Supporting Information Table 10) leads to only a slight change in the structural and vibrational properties. Interestingly, the all-electron basis sets DZVP-DFT (double-ζ on all atoms) and 6-311G/6-31G (triple-ζ on Fe and double-ζ on all other atoms) lead to an inferior description compared to the ECP basis sets. In these cases, the electronic structure has increased superoxo character with a shorter O−O bond and a larger O−O force constant. A triple-ζ all electron basis set (TZV in Supporting Information Table 10) is needed to obtain a comparable description to the ECP calculations. To test whether the substitution of the N4Py ligand by five ammonias is a valid approximation, calculations with the LanL2DZ basis set have been performed on two more sophisticated models. In $[Fe(Ime)_4(NH_3)(OOH)]^{2+}$, the four pyridine donors of the N4Py ligand, which are oriented cis to hydroperoxide, have been replaced by imines (Ime, $CH_2{=}NH$; cf. Supporting Information Figure 1 and Supporting Information Table 3). The Fe−N bond distances of the imines are shorter than those in $\tilde{\mathbf{1}}$, which is due to the differences in the radial distribution functions in sp^2 (imines) vs sp^3 (ammonia) hybrid functions. However, no improvement of the Fe−O and O−O force constants is achieved (cf. Table 5). Finally, the complete N4Py ligand was used in the calculation (see Supporting Information Figure 1 and Supporting Information Table 4), which leads to results very similar to those obtained for $[Fe(Ime)_4(NH_3)(OOH)]^{2+}$. Therefore, the usage of five ammonias instead of the large N4Py ligand is justified. In the following, the optimized structure from B3LYP/LanL2DZ of $\tilde{\mathbf{1}}$ is used for the calculation of the electronic structure and reactivity of **1**.

B.2. Description of the Electronic Structure of 1. The spin-unrestricted molecular orbital diagram of complex **1** (calculated for $\tilde{\mathbf{1}}$ using the B88P86 functional and a Slater-type triple-ζ (valence) basis set; see Experimental Section) is shown in Figure 4. The five d orbitals of iron are split into a three-fold degenerate t_{2g} set (d_{xy},d_{yz},d_{xz}) and a two-fold degenerate e_g set (d_{z^2},$d_{x^2-y^2}$) in an octahedral environment. In this case, the t_{2g} orbitals mediate π interactions with the ligands, and the e_g orbitals form σ bonds. In the ground-state electron configuration $[t_{2g}]^5$ of low-spin Fe(III), there is only one unoccupied t_{2g} function available, which is the β-d_{xz} LUMO (in the coordinate system shown in Figure 2). Hence, only the β-spin MOs contribute to π bonding. The e_g set is unoccupied, such that both α- and β-spin MOs participate in σ bonding. Since the spin-polarization effect on the e_g set of d orbitals is small, σ bonding is almost identical for the α and β sets, and the corresponding α and β MOs are very similar. Therefore, the β-spin MOs will exclusively be analyzed below.

The HOMO of the OOH^- ligand, π^*_v, acts as a π donor to the β-d_{xz} orbital of iron(III), which is the hole in the t_{2g} set, as described above. The resulting bonding combination of these orbitals, $\pi^*_v\_d_{xz}$ ($\beta\langle 31\rangle$, cf. Figure 5),[74] has about 27% iron contribution, corresponding to a very covalent bond (cf. Table 6). Accordingly, the antibonding combination, $d_{xz}\_\pi^*_v$ ($\beta\langle 34\rangle$), which is the LUMO of complex **1**, has a 30% admixture from the π^*_v orbital (in the following, this value is used as the calculated metal−ligand covalency). The CT band in the absorption spectrum of **1** around 18 200 cm^{-1} is assigned to the transition from $\pi^*_v\_d_{xz}$ to $d_{xz}\_\pi^*_v$. In the case of low-spin $[Fe(TPA)(OH_x)(OO^tBu)]^{x+}$, the corresponding CT transition is found at lower energy (~16 800 cm^{-1}). This trend relates to the fact that the hydrogen carries a larger positive charge than the central carbon of the *tert*-butyl group, which leads to a stronger polarization of the ROO^- ligand in **1**. Hence, the π^*_v orbital is shifted to lower energy in **1**, which increases the CT energy of the $\pi^*_v\_d_{xz}$ to $d_{xz}\_\pi^*_v$ transition.[75]

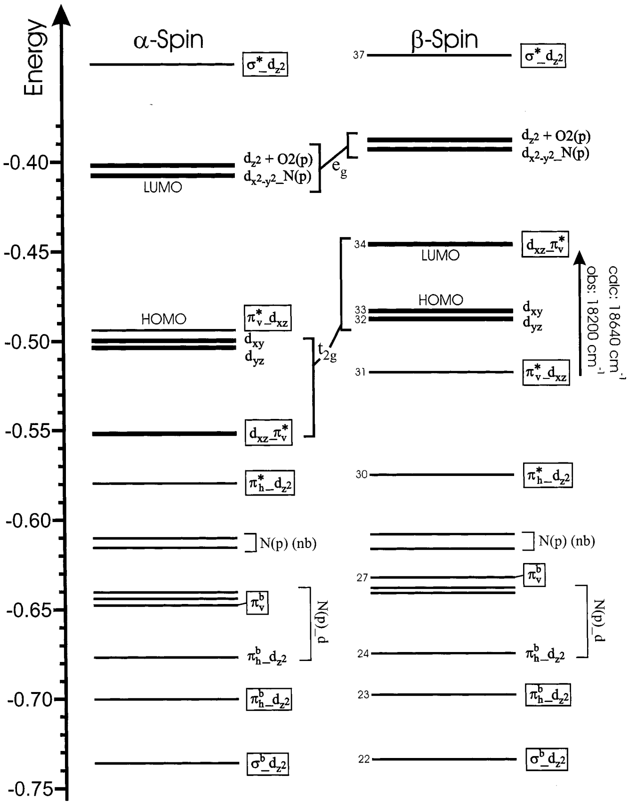

Figure 4. Molecular orbital diagram of $\tilde{\mathbf{1}}$ (in the coordinate system given in Figure 2) calculated with B88P86/triple-ζ basis. The nomenclature "*a_b*" indicates that orbital *a* interacts with *b* and that *a* has a larger contribution to the resulting MO. Important MOs corresponding to the donor orbitals of the hydroperoxo ligand are marked with a box. Thick lines correspond to MOs with large iron d contributions (>50%).

Next in energy to the π^*_v orbital of hydroperoxide is π^*_h, which forms a σ bond with the d_{z^2} orbital of iron. The corresponding bonding combination, $\pi^*_h\_d_{z^2}$ ($\beta\langle 30\rangle$), is shown in Figure 5 and has about 6% metal contribution (cf. Table 6). This interaction is stronger than in the case of low-spin $[Fe(TPA)(OH_x)(OO^tBu)]^{x+}$ (where π^*_h has ~3% metal admix-

---

(73) Kitajima, N.; Katayama, T.; Fujisawa, K.; Iwata, Y.; Moro-oka, Y. *J. Am. Chem. Soc.* **1993**, *115*, 7872−7873.

(74) Regarding the nomenclature: "$\pi^*_v\_d_{xz}$" denotes an MO that is a mixture of the orbitals π^*_v and d_{xz}; the one with the larger contribution to the MO comes first (in this example π^*_v). $\beta\langle 31\rangle$ refers to MO no. 31 with β spin.

(75) This should also decrease the covalent mixture of π^*_v and d_{xz}, which is in agreement with the observed lower relative donor strength of this CT transition in **1**. This effect is underestimated in the calculations, where the π^*_v covalency decreases from 36% in the low-spin Fe(III)−OO^{t}Bu complex[45] to 30% in the case of **1** (vide supra).

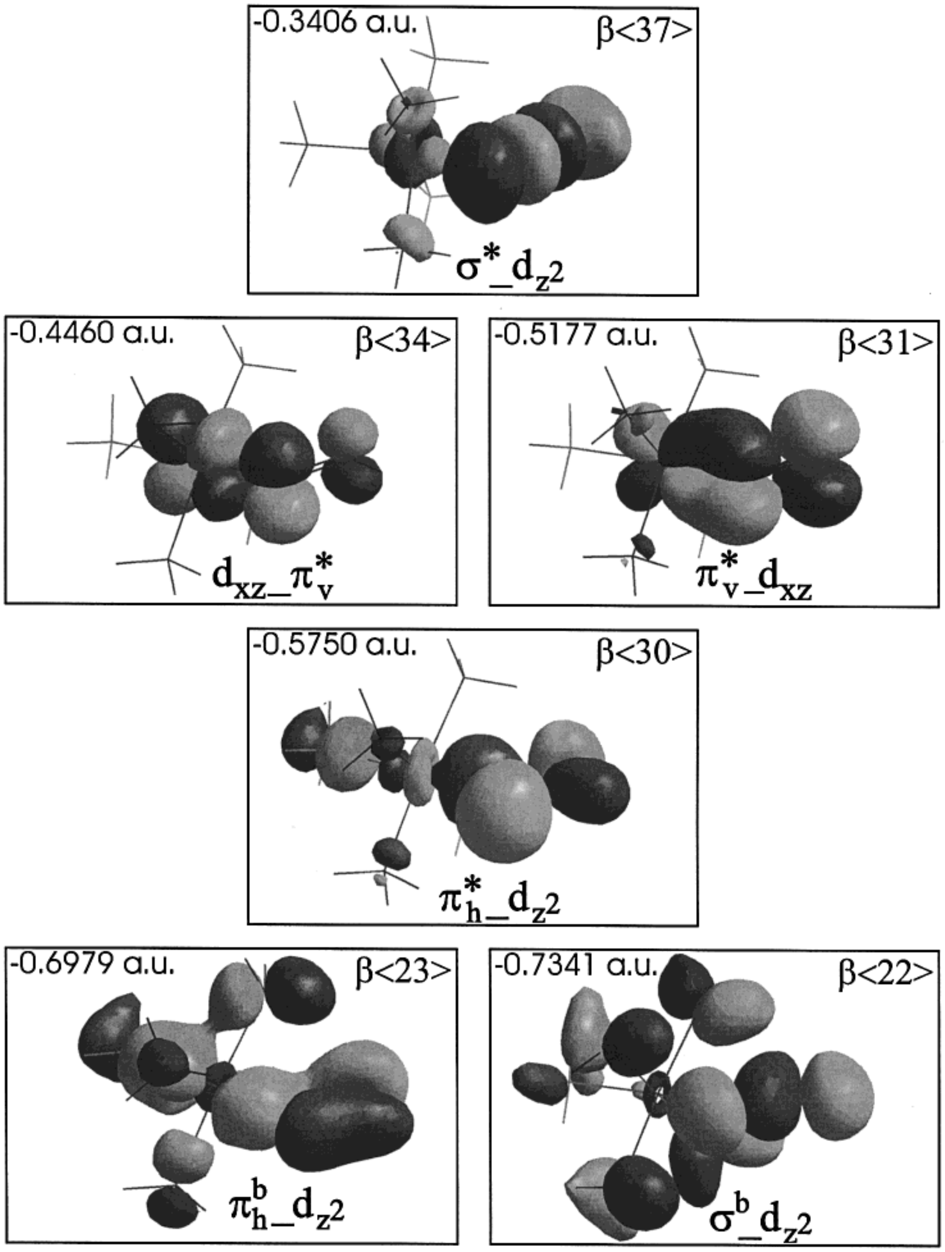

Figure 5. Contour plots of the molecular orbitals of $\tilde{\mathbf{1}}$ (cf. Figure 4 and Table 6) corresponding to the most important interactions of the hydroperoxo donor (π^*_v, π^*_h, π^b_h, and σ^b) and acceptor (σ^*) orbitals with the d functions of iron(III).

ture) and contributes to a strong Fe$-$O bond in **1**. This difference in bonding is due to the fact that π^*_h has no contribution from the hydrogen in the case of **1**. In contrast, π^*_h shows a C$-$O bonding interaction with the *tert*-butyl group which leads to polarization of this orbital away from the metal. Other σ interactions with d_{z^2} come from the O$-$O bonding orbitals π^b_h and σ^b of the hydroperoxide ligand which, however, are weak in the calculation. The corresponding bonding MOs, $\pi^b_h\_d_{z^2}$ ($\beta\langle 23\rangle$) and $\sigma^b\_d_{z^2}$ ($\beta\langle 22\rangle$), are shown in Figure 5. They have only about 1$-$2% metal contribution. The unoccupied orbital σ^* is mixed with the empty d_{z^2} function of iron and, hence, does not contribute to net bonding. This orbital is important since it is the potential electron acceptor of the Fe(III)$-$OOH unit (vide infra).

B.3. Excited-State Calculations. The experimentally derived assignments were evaluated using TD-DFT calculations within the Tamm$-$Dancoff approximation. The calculations predict the first two excited states at 7033 and 7750 cm^{-1}, respectively, to consist of the intra-t_{2g} transitions $d_{xy} \rightarrow d_{xz}\_\pi^*_v$ and $d_{yz} \rightarrow d_{xz}\_\pi^*_v$, both with very small predicted oscillator strength ($<10^{-5}$). The higher energy is in fair agreement with the experimentally observed MCD band at 6455 cm^{-1}, but the lower one appears to be predicted too high by $\sim$2500 cm^{-1} based on the EPR analysis (see section A.2), which means that the calculations predict the splittings within the t_{2g} set to be somewhat too axial. Starting at 13 475 cm^{-1}, the calculations predict a series of transitions that belong to the various multiplets that arise from $t_{2g} \rightarrow e_g$ single excitations.[10] However, all of these transitions have calculated oscillator strengths of $<10^{-4}$ and are not likely to be observable in the experimental spectrum. The important CT transition $\pi^*_v\_d_{xz} \rightarrow d_{xz}\_\pi^*_v$ is predicted at 20 402 cm^{-1},[76] with an oscillator strength of 0.0198, which is

---

[76] From ΔSCF calculations, the energy of this transition is predicted to be at 18 640 cm^{-1} (cf. Figure 4).

Table 6. Charge Contributions of Important β Orbitals of $\tilde{\mathbf{1}}$ Calculated with B88P86/Triple-ζ Basis

no.	label	energy (Hartree)	Fe d	O2 s	O2 p	O3 s	O3 p	H s	ΣN s + p
$\beta\langle 37\rangle$	σ^{*}_d_{z^2}	−0.3406	6	2	42	3	35	1	2
$\beta\langle 36\rangle$	d_{z^2} + O2(p)[a]	−0.3891	61	1	13	0	3	0	16
$\beta\langle 35\rangle$	$d_{x^2-y^2}$_N(p)	−0.3923	69	0	0	0	0	0	26
$\beta\langle 34\rangle$	d_{xz}_π_v^{*} (LUMO)	−0.4460	67	0	23	0	7	0	1
$\beta\langle 33\rangle$	d_{xy} (HOMO)	−0.4843	93	0	1	0	1	0	0
$\beta\langle 32\rangle$	d_{yz}	−0.4870	92	0	0	0	3	0	0
$\beta\langle 31\rangle$	π_v^{*}_d_{xz}	−0.5177	27	0	30	0	37	0	1
$\beta\langle 30\rangle$	π_h^{*}_d_{z^2}[a]	−0.5750	6	2	58	2	15	2	11
$\beta\langle 27\rangle$	π_v^{b}	−0.6322	3	0	33	0	29	0	23
$\beta\langle 26\rangle$	N(p)_d_{z^2}	−0.6380	16	0	2	1	6	0	58
$\beta\langle 25\rangle$	N(p)_$d_{x^2-y^2}$	−0.6409	28	0	1	0	1	0	59
$\beta\langle 24\rangle$	N(p)_d_{z^2} + π_h^{b}_d_{z^2}[a]	−0.6746	10	0	7	2	15	0	52
$\beta\langle 23\rangle$	π_h^{b}_d_{z^2}[a]	−0.6979	2	0	21	5	24	2	32
$\beta\langle 22\rangle$	σ^{b}_d_{z^2}[a]	−0.7341	1	2	19	0	25	5	27

[a] The charge contributions are the averages of α and β orbitals (both are very similar) to illustrate σ bonding.

Table 7. Thermodynamics of Homolytic Cleavage of the O−O Bond in $\tilde{\mathbf{1}}$ and $\tilde{\mathbf{2}}$ (Calculated with B3LYP)

reactant	product [a]	ΔE (kcal/mol) LanL2	ΔE (kcal/mol) + Solv[c]	ΔE (kcal/mol)[b] TZV	ΔE (kcal/mol)[b] + Solv[c]	$-T\Delta S$ (kcal/mol)	ZPCE (kcal/mol)
$[Fe(NH_3)_5(OOH)]^{2+}$	$S = 1$	46.1	35.8	40.3	29.7	−12.4	−4.6
$\tilde{\mathbf{1}}$ ($S = 1/2$)	$S = 2$[d]	52.4	45.9	43.2	36.4	−15.6	−7.0
$[Fe(NH_3)_4(OH)(OOH)]^{+}$	$S = 1$	37.1	30.8	31.5	25.0	−11.0	−4.2
$\tilde{\mathbf{2}}$ ($S = 1/2$)	$S = 2$[d]	39.1	34.7	30.3	25.7	−11.9	−6.1
ABLM″ ($S = 1/2$)	$S = 1$	34.5	29.9	29.4	26.8	−10.3	−3.9

[a] Spin state of the Fe(IV)═O complex; the •OOR radical has $S' = 1/2$. Total spin: $S_{tot} = S \pm S'$. [b] Shifts of the energies of the different spin states relative to each other are observed with TZV. This is due to the fact that the used geometries are *not* optimized for TZV. [c] Solv: including a solvent sphere in the calculation using the polarized continuum model (PCM) and acetonitrile ($\tilde{\mathbf{1}}$ and $\tilde{\mathbf{2}}$) and water (ABLM) as solvent; entropy ($T = 298$ K) and zero point correction energy (ZPCE) calculated using the LanL2DZ basis set. [d] Spin-forbidden reaction.

Chart 2

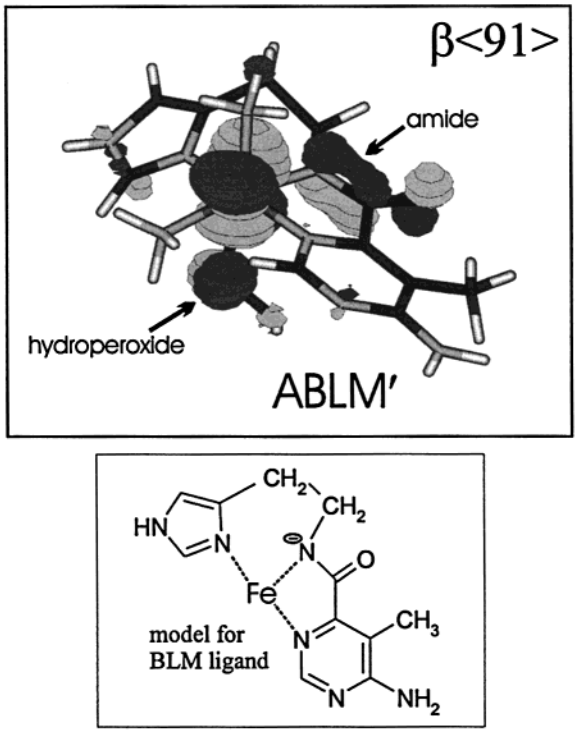

close to the observed bands 2 and 3 that occur at 17 542 and 19 149 cm^{-1}, respectively, having a combined oscillator strength of ~0.02 (cf. Table 3). Importantly, the TD-DFT calculations give evidence for extensive mixing of the CT transition with nearby $t_{2g} \rightarrow e_g$ excitations. The CT state at 20 402 cm^{-1} has only 69% CT character and 31% $t_{2g} \rightarrow e_g$ character. On the higher energy side of this band, one mainly $t_{2g} \rightarrow e_g$ transition calculated at 22 362 cm^{-1} gains intensity, with an oscillator strength of ~0.003. To higher energy, no transition up to ~33 000 cm^{-1} gains appreciable intensity. Thus, band 5, which has been assigned as a pyridine-to-Fe(III) CT, is not modeled by the calculations that use simple ammonia ligands. The π_h^{*}_$d_{z^2} \rightarrow d_{z^2}$_$\pi_h^{*}$ transition that is expected to have reasonable intensity must occur to higher energy but is not found within the first 20 excited states treated in the calculations. There are, however, two additional π_v^{*}_$d_{xz} \rightarrow e_g$ CT transitions predicted around 26 000 cm^{-1} that have small transition densities and, hence, small predicted oscillator strengths ($<5 \times 10^{-4}$) due to the poor relative orientations of the orbitals involved. Hence, they are not observed in the experimental spectrum.

In summary, the TD-DFT calculations predict extensive CT/d−d mixing within the dominant π_v^{*}_$d_{xz} \rightarrow d_{xz}$_$\pi_v^{*}$ CT transition (bands 2 and 3). The experimentally observed ratio is ~50:50, whereas a ~70:30 mixing is found in the calculations. These calculations indicate that the model used to explain the observed pseudo-**A** term in the MCD spectrum is reasonable. The calculated total oscillator strengths and band positions are in reasonable agreement with the data supporting the experimentally derived assignments.

B.4. Thermodynamics of Homolytic O−O Bond Cleavage. Complex **1** has been shown to undergo homolytic cleavage of the O−O bond,[21] which is the same reaction that is observed for low-spin $[Fe(TPA)(OH_x)(OO^tBu)]^{x+}$ [41,43−45] (see Introduction). To investigate the O−O bond homolysis for low-spin Fe(III)−OOH complexes, DFT calculations have been applied to model system $\tilde{1}$ for the reaction:

$$[Fe(NH_3)_5(OOH)]^{2+} \rightarrow [Fe(NH_3)_5(O)]^{2+} + \bullet OH \qquad (1)$$

The structures of all species have been fully optimized with B3LYP/LanL2DZ (see Experimental Section). Using the LanL2DZ basis set, reaction energies of about 50 kcal/mol are obtained for the $[Fe(NH_3)_5(O)]^{2+}$ product in the spin states $S = 1, 2$, as given in Table 7. The spin state $S = 0$ has not been considered for the Fe(IV)═O intermediate, because it has been shown to be energetically very unfavorable.[45] Taking into account solvent effects leads to a large reduction of these reaction energies, as shown in Table 7. Applying the all-electron triple-ζ TZV basis set on the LanL2DZ structures and including solvation, the endothermicity of the O−O homolysis decreases to 30 kcal/mol for the Fe(IV)═O product with $S = 1$. Taking into account zero point energy corrections and entropy effects, a free reaction energy of about +15 kcal/mol is obtained. Considering that **1** decays experimentally on a time scale of minutes at room temperature, this number is reasonable.

To directly compare low-spin Fe(III)−OOH and Fe(III)−OO^{t}Bu complexes (see Discussion), the O−O bond homolysis has also been investigated for low-spin $[Fe(TPA)(solv)(OOH)]^{x+}$ (**2**). The model system low-spin $[Fe(NH_3)_4(OH)(OOH)]^{+}$ ($\tilde{\mathbf{2}}$) has been used which has hydroxide cis to the ROO$^-$ ligand

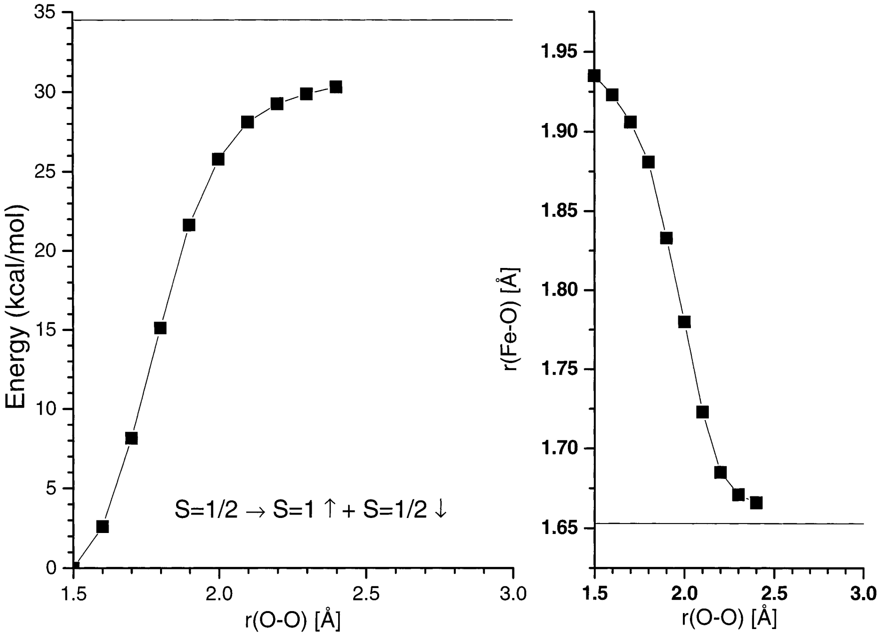

Figure 6. Reaction coordinate for the homolytic cleavage of the O−O bond calculated for ABLM′ ($S = {}^1/_2$) with B3LYP/LanL2DZ. On the left, the PES is given relative to the reactant set to 0 kcal/mol. The horizontal line on the top represents the energy of the products at infinite distance for Fe(IV)═O with $S = 1$. On the right, the change of the Fe−O bond length along the O−O reaction coordinate is given. The horizontal line on the bottom represents the Fe−O distance in the Fe(IV)═O product ($S = 1$).

like the model $[Fe(NH_3)_4(OH)(OO^tBu)]^+$ that has been used for the low-spin Fe(III)−OO^{t}Bu complex in ref 45. The following reaction is investigated:

$$[Fe(NH_3)_4(OH)(OOH)]^+ \rightarrow [Fe(NH_3)_4(OH)(O)]^+ + \bullet OH \qquad (2)$$

The structure of $\tilde{\mathbf{2}}$ has been fully optimized using B3LYP/LanL2DZ, and the geometric parameters, frequencies, and spin densities obtained are given in Table 5 and Supporting Information Table 10. The optimized structures of the corresponding Fe(IV)═O products for $S = 1, 2$ are taken from ref 45. Table 7 shows the results for O−O homolysis of $\tilde{\mathbf{2}}$. Using the TZV basis set and including solvent effects, a reaction energy of +25 kcal/mol is obtained. This number is reduced to a free energy of about +10 kcal/mol when zero point energy corrections and entropy are taken into account.

B.5. Comparison with Activated Bleomycin. In the case of ABLM, it has been shown that the hole in the $[t_{2g}]^5$ subshell of iron is rotated away from hydroperoxide, toward the amide donor[10] (see Discussion). Using a simplified model for ABLM as given in ref 10 and optimizing all Fe−ligand bond lengths as well as the Fe−OOH subunit with DFT (the structure of this model, ABLM′, is shown in Supporting Information Figure 3), a qualitatively comparable result is obtained. Chart 2 shows the singly occupied t_{2g} orbital of this model, which is rotated away from the hydroperoxide π^*_v orbital and is essentially nonbonding to the ligands. In the following, the effect of the altered electronic structure of ABLM on the homolytic cleavage of the O−O bond is examined.

For the calculation of the thermodynamics of O−O bond homolysis, model ABLM′ has been fully optimized in order to determine the entropy and the zero point correction energy (ZPCE) contribution to the total energy. Table 7 shows that homolytic cleavage of the O−O bond for this model, ABLM″ (see Supporting Information Figure 3),[77] is endothermic by about 27 kcal/mol (using the TZV basis set and including solvation). In comparison, equivalent reaction energies are obtained for ABLM′ (the difference is ~2 kcal/mol and, hence, within the tolerance of the DFT calculations). Taking into account the entropy and ZPCE contribution, a free reaction energy of about +12 kcal/mol is obtained. The reaction coordinate for O−O bond homolysis in ABLM shown in Figure 6, left, has been calculated using model ABLM′. The energy increases continuously along the reaction coordinate leading to the dissociation products. This reflects the endothermicity of the O−O bond homolysis of about +35 kcal/mol, as described above (not including solvation, entropy, and ZPCE contributions as given in Table 7). Importantly, no additional barrier due to a transition state is observed for this reaction. This is in agreement with results for low-spin $[Fe(TPA)(OH_x)(OO^tBu)]^{x+}$ (cf. ref 46). As in this case, the redox-active orbitals interact along the reaction coordinate, which leads to a smooth conversion of the reactants into products. This is also reflected by the gradual shortening of the Fe−O distance on elongation of the O−O bond, as shown in Figure 6, right. In summary, these results indicate that homolytic cleavage of the O−O bond is a thermodynamically and kinetically accessible but slow (due to the endothermicity) reaction for ABLM′.

Discussion

The resonance Raman spectrum of low-spin $[Fe(N4Py)(OOH)]^{2+}$ (**1**) shows peaks at 790 and 632 cm^{-1} that have been assigned to the O−O and Fe−O stretches, respectively.[49] From

---

(77) Full optimization of ABLM′ leads to only minor changes of the overall structure of the BLM ligand. However, the electronic structure of the resulting model ABLM″ is comparable to that of complexes **1** and **2**, where the hole in the $[t_{2g}]^5$ subshell of iron overlaps with hydroperoxide. This is manifested in a decreased Fe−O bond length by 0.1 Å compared to ABLM′. Therefore, the orientation of the singly occupied t_{2g} orbital is determined by the BLM ligand as a subtle interplay of ligand orientation and metal−ligand bond lengths.

normal coordinate analysis (NCA), force constants have been determined to be 3.05 mdyn/Å for the O−O bond and 3.62 mdyn/Å for the Fe−O bond. This corresponds to a strong Fe−O bond and a weak O−O bond. The UV−vis spectrum of **1** shows a moderately intense absorption around 550 nm, which is assigned to a CT transition from the π_v^* orbital of hydroperoxide to the singly occupied t_{2g} orbital of low-spin Fe(III), corresponding to an Fe−O π bond. With the help of DFT calculations, additional contributions to the Fe−O bond have been identified. These correspond to σ interactions between the π_h^*, π_h^b, and σ^b orbitals of hydroperoxide and an e_g function of iron(III). Compared to experiment, the DFT calculations overestimate the π covalency and underestimate the σ interaction from the O−O bonding orbitals π_h^b and σ^b. This leads to the observed discrepancies between the calculated ($f_{O-O} = 3.93$ mdyn/Å, $f_{Fe-O} = 3.25$ mdyn/Å) and experimental ($f_{O-O} = 3.05$ mdyn/Å, $f_{Fe-O} = 3.62$ mdyn/Å) force constants. Low-spin [Fe(TPA)(solv)(OOH)]$^{x+}$ (**2**) has spectroscopic properties that are very similar to those of complex **1**: the O−O and Fe−O stretching vibrations have comparable energies (789 and 626 cm^{-1}, respectively) and a medium intense CT transition is observed in the visible region of the absorption spectrum that is centered around 540 nm ($\epsilon = 1000$ M^{-1} cm^{-1}).[49] This clearly demonstrates that the electronic structure of **2** is comparable to that of **1**.

The results from spectroscopy indicate that the electronic structures of the Fe(III)−OOR subunit in **1** and low-spin [Fe(TPA)(OH$_x$)(OO^{t}Bu)]$^{x+}$ (cf. ref 45) are very similar. The analysis of the vibrational data shows that both complexes have a strong Fe−O bond and a weak O−O bond with similar force constants. This indicates that the overall bonding between Fe(III) and peroxide is comparable in these systems. However, the covalencies involved in the individual orbital interactions are different. The π bond between Fe(III) and the peroxo ligand is distinctly weaker in **1**. This is reflected by the relative donor strength of the corresponding CT transition in the visible region, which is reduced by 50%. This decrease in π bonding in **1** is compensated by a stronger σ interaction of the π_h^* orbital with an e_g function of Fe(III). This leads to an overall comparable amount of donation from the π* orbitals in both systems. Based on this, the σ interaction from the O−O bonding orbitals π_h^b and σ^b must be comparable in **1** and low-spin [Fe(TPA)(OH$_x$)(OO^{t}Bu)]$^{x+}$, leading to the similar Fe−O and O−O force constants and, hence, bond strengths.

Both low-spin [Fe(TPA)(OH$_x$)(OO^{t}Bu)]$^{x+}$ and **1** have been shown to undergo homolytic cleavage of the O−O bond, which therefore seems to be a general reaction channel for low-spin Fe(III)−OOR complexes.[15,21,41−47] This reaction has been calculated by DFT to be approximately thermoneutral in terms of free energy for low-spin [Fe(TPA)(OH$_x$)(OO^{t}Bu)]$^{x+}$.[45] In comparison, O−O homolysis is calculated to be endothermic by about +10 kcal/mol for **2** (using hydroxide as the sixth ligand) and +15 kcal/mol for **1**. The shift to positive free reaction energies for the Fe(III)−OOH systems is mainly due to two effects. First, the resulting •OR radical is stabilized by hyperconjugation for R = ^{t}Bu compared to R = H, as shown in Chart 3, which increases reaction energies for the hydroperoxo complexes by about 6 kcal/mol. Moreover, the presence of the hydroxo ligand in the Fe(III)−OO^{t}Bu complex and **2** leads to a stabilization of the Fe(IV)=O product compared to **1**, which only has a set of neutral N-donor ligands. This accounts for most of the 5 kcal/mol increase in reaction energy for **1** compared to **2**. These trends are in qualitative agreement with experiment, where **1** has a longer lifetime than low-spin [Fe(TPA)(OH$_x$)(OO^{t}Bu)]$^{x+}$ at room temperature.[78] Kinetically, it has been found that there is no barrier for O−O homolysis in low-spin [Fe(TPA)(OH$_x$)(OO^{t}Bu)]$^{x+}$.[46] The same can be expected for low-spin Fe(III)−OOH complexes due to their closely related electronic structures having an overall identical Fe(III)−peroxo bond (vide supra). In summary, the homolytic cleavage of the O−O bond is a thermodynamically and kinetically accessible reaction for low-spin Fe(III)−OOH complexes. The rate is slower compared to those of analogous alkylperoxo complexes due to less favorable reaction energies.

Chart 3

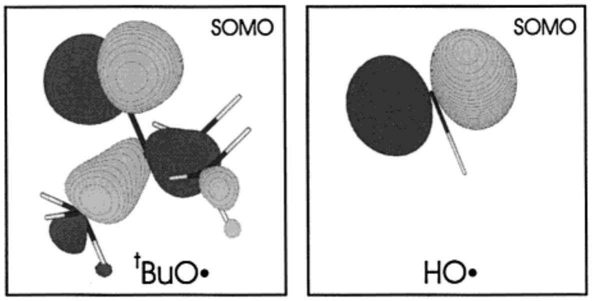

Activated bleomycin (ABLM) is also a low-spin Fe(III)−OOH complex. However, its spectroscopic properties and electronic structure are different from those of **1** and **2**. This originates from a rotation of the hole in the t_{2g} shell away from the hydroperoxo ligand, which removes the Fe−O π bond and, hence, the corresponding CT transition in the visible region.[10] These results are in qualitative agreement with DFT calculations on an ABLM model (ABLM′) which show a rotation of the singly occupied t_{2g} orbital toward the amide donor of the BLM ligand. This difference in the electronic structure compared to those of **1** and **2** is also reflected by an increase of the Fe−O bond length by ~0.1 Å in ABLM′. To determine whether ABLM is capable of O−O homolysis, DFT calculations have been applied. The free reaction energy obtained of +12 kcal/mol is comparable to the values calculated for **1** and **2**. In addition, the potential energy surface (PES) has been calculated to evaluate the effect of the rotated t_{2g} shell on the kinetics of this reaction. No barrier is observed along the reaction coordinate, and no perturbation of the PES due to the orbital rotation occurs. This indicates that the difference in the electronic structure of ABLM compared to those of complexes **1** and **2** does not play a significant role in O−O homolysis. On elongation of the O−O bond in ABLM′, the t_{2g} hole rotates back toward the hydroperoxo ligand early on the reaction coordinate; hence, O−O homolysis proceeds in a similar way in ABLM and models **1** and **2**. Note that the effect of this orbital misalignment might be underestimated in the DFT calculations since the rotation of the t_{2g} hole can be expected to be more pronounced in a more accurate model of ABLM.

These results show that ABLM should be thermodynamically and kinetically competent to undergo O−O homolysis. This is supported by the fact that the complex [Fe(PMA)(OO^{t}Bu)]$^+$ with the PMA ligand, which closely models BLM, shows homolytic

---

(78) Que, L., Jr., unpublished data.

cleavage of the O−O bond.[15] Experimentally, a different reactivity has been observed for ABLM. A large kinetic isotope effect (KIE), $k_H/k_D \approx 2-7$, has been determined for the reaction of ABLM with DNA,[40] which is in contrast to the small KIEs that have been observed for free •OH radicals[79−81] and also for the radical-based reaction of CoBLM with DNA.[40,82] This argues for a direct attack of ABLM on DNA, where the low-spin Fe(III)−OOH species directly abstracts an H atom from the sugar moiety.[10] As described in the Introduction, this reaction is closely related to O−O homolysis. But whereas in the latter case the cleavage of the O−O bond precedes the attack of the resulting •OH radical on the substrate, the direct H atom abstraction represents the concerted version of this process. The direct reaction should therefore be kinetically favorable, since the energy required for the O−O bond cleavage is partially compensated by the formation of the O−H bond. This lowers the energy barrier for the total reaction, which originates from the endothermicity of the O−O homolysis step. This point needs further study in order to quantitatively determine the energetics of the total reaction coordinate. Another important factor that promotes the direct reaction in ABLM is its high affinity for the DNA substrate and the geometry of the resulting ABLM−DNA adduct, which is well oriented for H atom abstraction by the σ^* orbital of hydroperoxide (cf. the structure of the CoBLM−DNA adduct determined with NMR spectroscopy[83]). In summary, these results indicate that ABLM should potentially be capable of undergoing O−O homolysis, but the direct H atom abstraction is kinetically favorable in the reaction with DNA.[84] In contrast, complex **1** does not appear to show a direct reaction with substrates but undergoes homolytic cleavage of the O−O bond (vide supra). The occurrence of O−O homolysis in this case might be attributed to the lack of a fixed oxidant−substrate geometry which sets the system up for direct attack on the C−H bond by the σ^* orbital of the Fe(III)−OOH unit (cf. Figure 5, top). Alternatively, the rotation of the t_{2g} hole away from the hydroperoxo ligand in ABLM might be more severe than indicated in the calculations (vide supra) and might lead to some decrease in its rate of O−O homolysis. This would also favor the direct reaction for ABLM.

Acknowledgment. This work was supported by the National Institutes of Health (GM-40392 to E.I.S. and GM-33162 to L.Q.). N.L. thanks the Deutscher Akademischer Austauschdienst (DAAD) for a postdoctoral fellowship. F.N. thanks the Deutsche Forschungsgemeinschaft (DFG) for postdoctoral (1997−1999) and Habilitation stipends (1999−2001). Dr. Robert Szilagyi is acknowledged for a molecular mechanics (MM) geometry optimization of the complete $[Fe(N4Py)(OOH)]^{2+}$ molecule, which was used as a starting point for the DFT calculations.

Supporting Information Available: Figures showing the fully optimized structures of low-spin $[Fe(Ime)_4(NH_3)(OOH)]^{2+}$, low-spin $[Fe(N4Py)(OOH)]^{2+}$, low-spin $[Fe(NH_3)_4(OH)(OOH)]^{+}$ ($\tilde{\mathbf{2}}$), ABLM′, ABLM″, and the Fe(IV)═O intermediate that results from O−O homolysis in ABLM; Cartesian coordinates of the optimized structures of low-spin $[Fe(NH_3)_5(OOH)]^{2+}$ ($\tilde{\mathbf{1}}$) and the six species mentioned above; complete force field of $\hat{\mathbf{1}}$ used for NCA; and geometric and vibrational properties as well as Mulliken charges and spin densities for low-spin $[Fe(NH_3)_5(OOH)]^{2+}$ optimized with different basis sets and the other low-spin Fe(III)−OOH species (PDF). This material is available free of charge via the Internet at http://pubs.acs.org.

JA012621D

---

(79) Buxton, G. V.; Greenstock, C. L.; Helman, W. P.; Ross, A. B. *J. Phys. Chem. Ref. Data* **1988**, 513−886.

(80) Khenkin, A. M.; Shilov, A. E. *New J. Chem.* **1989**, 659−667.

(81) Sawyer, D. T.; Kang, C.; Llobet, A.; Redman, C. *J. Am. Chem. Soc.* **1993**, *115*, 5817−5818.

(82) Tan, J. D.; Hudson, S. E.; Brown, S. J.; Olmstead, M. M.; Mascharak, P. K. *J. Am. Chem. Soc.* **1992**, *114*, 3841−3853.

(83) Wu, W.; Vanderwall, D. E.; Teramoto, S.; Lui, S. M.; Hoehn, S. T.; Tang, X.-J.; Turner, C. J.; Boger, D. L.; Kozarich, J. W.; Stubbe, J. *J. Am. Chem. Soc.* **1998**, *120*, 2239−2250 and references therein.

(84) Note that ABLM decays in the absence of DNA with a pseudo-first-order rate that is comparable to the rate of reaction with DNA.[4] This indicates that the decay of ABLM might proceed through a similar reaction, for example the direct abstraction of an H atom from the BLM ligand.

(85) Redington, R. L.; Olson, W. B.; Cross, P. C. *J. Chem. Phys.* **1962**, *36*, 1311−1326.

(86) Oakes, J. M.; Harding, L. B.; Ellison, G. B. *J. Chem. Phys.* **1985**, *83*, 5400−5406.

(87) Baldwin, M. J.; Ross, P. K.; Pate, J. E.; Tyeklar, Z.; Karlin, K. D.; Solomon, E. I. *J. Am. Chem. Soc.* **1991**, *113*, 8671.